ORIGINAL ARTICLE

Investigation on the Mechanical Properties and Shape Memory Effect of Landing Buffer Structure Based on NiTi Alloy Printing

Zhenglei Yu[1,2], Renlong Xin[2], Zezhou Xu[2], Yining Zhu[3], Xiaolong Zhang[2], Shijie Hao[4], Zhihui Zhang[2*] and Ping Liang[2*]

Abstract

With the deepening of human research on deep space exploration, our research on the soft landing methods of landers has gradually deepened. Adding a buffer and energy-absorbing structure to the leg structure of the lander has become an effective design solution. Based on the energy-absorbing structure of the leg of the interstellar lander, this paper studies the appearance characteristics of the predatory feet of the *Odontodactylus scyllarus*. The predatory feet of the *Odontodactylus scyllarus* can not only hit the prey highly when preying, but also can easily withstand the huge counter-impact force. The predatory feet structure of the *Odontodactylus scyllarus*, like a symmetrical cone, shows excellent rigidity and energy absorption capacity. Inspired by this discovery, we used SLM technology to design and manufacture two nickel-titanium samples, which respectively show high elasticity, shape memory, and get better energy absorption capacity. This research provides an effective way to design and manufacture high-mechanical energy-absorbing buffer structures using bionic 3D printing technology and nickel-titanium alloys.

Keywords Bionic protective structure, *Odontodactylus scyllarus*, NiTi alloy, 3D printing, Numerical simulation, Recoverability

1 Introduction

Soft landing on the surface of asteroids is a key challenge in the field of deep space exploration. In the case of a lunar landing, the spacecraft needs to land without aerodynamic deceleration on the surface of the moon. Thus, it must rely on its own propulsion system to gradually reduce its speed so that it can land safely in a predetermined area. The landing speed cannot be reduced to zero when the lander has a full contact with the lunar surface, and the lander is subjected to heavy impact loads upon landing. Therefore, it is necessary to add an auxiliary landing buffer system to absorb the remaining kinetic energy over a limited distance. Zeng et al. [1] modified the dynamics analysis model by using the groun experiment resulting from a simulated lander and found that the structure of the lander and the flexibility of the buffer mechanism have a great impact on the buffer performance. Yan et al. [2] analyzed the factors that influence the landing buffer characteristics in the soft-landing process of a reusable vehicle for vertical taking-off and landing. The simulation analysis of the honeycomb buffer was carried out, and the deformation and buffering characteristics in the process of honeycomb crushing were discussed. Van et al. [3] developed and proposed a

*Correspondence:
Zhihui Zhang
zhzh@jlu.edu.cn
Ping Liang
liangping@jlu.edu.cn
[1] State Key Laboratory of Automotive Simulation and Control, Jilin University, Changchun 130022, China
[2] Key Lab of Bionic Engineering, Ministry of Education, Jilin University, Changchun 130022, China
[3] Agriculture College, Yanbian University, Yanji 133002, China
[4] State Key Laboratory of Heavy Oil Processing, China University of Petroleum, Beijing 102249, China

Yu *et al. Chinese Journal of Mechanical Engineering*   (2023) 36:104

Page 2 of 10

fast and parallel simulation of the lander/rover bounce deployment on asteroids or comets. Besides, they also studied the collision and contact motion between a probe with arbitrary shape/inertia and a target body. At present, large numbers of domestic and foreign scholars have done a lot of research on landing modes for controlling landers and impact buffers during landing, and the research on the supporting legs of landers is mainly focused on the research [4–8] and development of the mechanical structures [6, 9, 10]. However, there is an urgent need for research on the structure design of the supporting legs and its reusability.

In the lengthy process of biological evolution, a variety of organisms gradually develops unique structures to adapt to the environment [11–13]. These structures and functions tend to be perfect, providing a reference for solving many modern engineering problems. For example, the finch-tailed mantis shrimp is known as the "boxer" of the sea world. Its developed grazing feet (PF) can not only crush prey at speeds of up to 80 km/h, but also disperse and deflect the energy produced by the impact. Due to its unique structure to realize the impact of energy absorption, shrimp can withstand the impact of more than 700 N [14–16]. Therefore, the research on the mechanism of load absorption in the forefeet structure of mantis shrimp will have an great impact on the development of the field of shock absorption and cushioning structure. Patek et al. [17] studied the energy release process of mantis shrimp during a single punch and the elastic mechanism of mantis shrimp which is composed of exoskeleton and controlled by latch mechanism. James [18] studied the morphological characteristics of feet predation of mantis shrimp. Guo et al. [19] designed a corresponding bionic sandwich structure for armor protection. As shown in Figure 1, the obvious sandwich structure of the mantis shrimp feet makes it incredibly impact resistant, which provides a good model for us to design impact resistant structures.

Due to its excellent shape memory effect and superelasticity, NiTi has attracted wide attention of scholars at home and abroad [20]. It's their poor machinability that limits its application in structural parts. In this regard, many scholars use Additive Manufacturing (AM) to manufacture NiTi alloy structures and parts [21–26]. Through AM technology, structural parts can be printed directly, avoiding the post-processing process, and components can be directly formed. SLM-NiTi is widely used in porous structures owing to its excellent biocompatibility and elastic modulus close to the human body [27–29]. However, the research on bionic structures with shape memory effect and hyperelasticity is relatively scarce. Ma et al. [30] reported the bionic structure of NiTi crab claws by using SLM, and
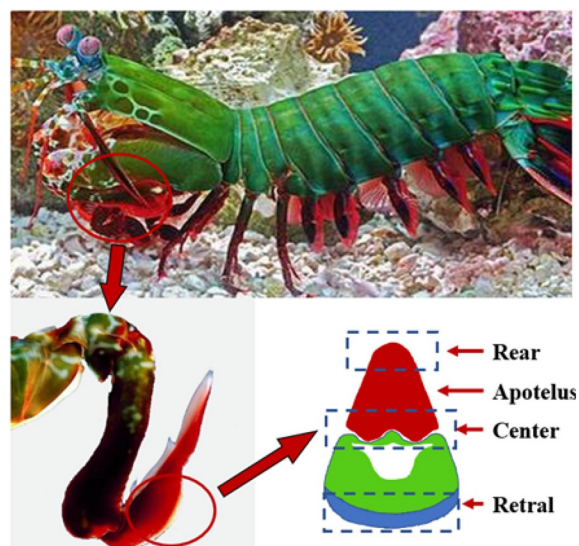

Figure 1 Schematic diagram of the Predatory Feet (PF)

separately studied the effects of different pore distribution forms on energy absorption. It was found that three different pore distribution modes significantly improved the toughness of Nitinol part and showed similar energy absorption capability. The recovery rate of NiTi structure parts found by Xiong et al. [31] can reach 99% under 50% large deformation. SLM-NiTi has a profound research value in bionic structure and shape memory effect.

This paper aims to study a SLM-NiTi bionic energy-absorbing structure, which can be recoveried and recycled after heating. Taking Odontodactylus scyllarus feet prey sandwich structure as the bionic research object, the model was established by using CATIA, a 3D modeling software, and the simulation analysis was carried out by finite element analysis software under the load condition. Then the structure prototype was prepared by the 3D printing technology, and the mechanical properties of the prototype were experimented. By comparing with the simulation data, the stress-strain relationship of the structural model under axial compression and unloading under different working conditions was analyzed, and the bearing capacity and recovery performance of the model were studied. The accuracy of the simulation analysis and the effectiveness of the method were verified by comparing with the experimental results. Then the Cell Structure (CS) was upgraded to the and the Double Layer Structure (DLS), and the finite element model and solid model of the DLS were established. By numerical simulation and experimental experiment, the absorbing capacity of the DLS under the same loading and unloading conditions was obtained.

Yu *et al. Chinese Journal of Mechanical Engineering*   (2023) 36:104

Page 3 of 10

2 Materials and Methods

2.1 Material Selection

$Ni_{50.8}Ti_{49.2}$ alloy powder ($Ni_{50.8}Ti_{49.2}$ powders with particle size between 13 μm and 53 μm prepared by electrode induction-molten gas atomization (EIGA) process) was selected for printing. In the printing process, high purity argon gas is used as the protective gas to reduce the oxygen content in the manufacturing chamber.

Figure 2 shows the characteristic analysis of the alloy powder we selected. It can be seen from Figure 2(a) that the alloy powder we used has a high sphericity, which is conducive to the melting of the metal powder bed. Figure 2(b) shows the particle size distribution of $Ni_{50.8}Ti_{49.2}$ alloy powder, from which we can see that the particle size of the powder less than 22.2 μm accounts for 10%, and the particle size greater than 58.1 μm accounts for 10%. The particle size distribution of this batch of powder has a wide main peak near the average particle size $d_{50} = 36.8$ μm, which indicates that the powder has a good uniformity. Figure 2(c) shows the DSC curve of $Ni_{50.8}Ti_{49.2}$ powder. The initial temperature (M_s) and termination temperature (M_f) of martensitic phase transformation are 24.8 °C and −16.7 °C, respectively. The initial temperature (A_s) and termination temperature (A_f) of austenitic phase transformation are − 25.3 °C and 54.9 °C, respectively.

2.2 Architecture of the Energy-Absorbing Structures

It was observed under the Stereo Microscope that the PF of Odontodactylus scyllarus has a cone-shaped structure. According to the bionic design principle, taking Odontodactylus scyllarus as the biological model, the landing buffer bionic model was established by using CATIA software. The outer width (L), overall height (H), support thickness (T) and support width (W) of the CS are 26 mm, 18 mm, 0.5 mm, and 3 mm, respectively. The width (L), overall height (H), support thickness (T) and support width (W) of the DLS model are 23 mm, 17 mm, 0.6 mm and 1.5 mm, respectively (see Table 1).

As shown in Table 2, in order to reduce the cost and time of real-time experiments, and to conduct further research, the nonlinear explicit finite element (FE) code LS-DYNA is employed to simulate the uniform
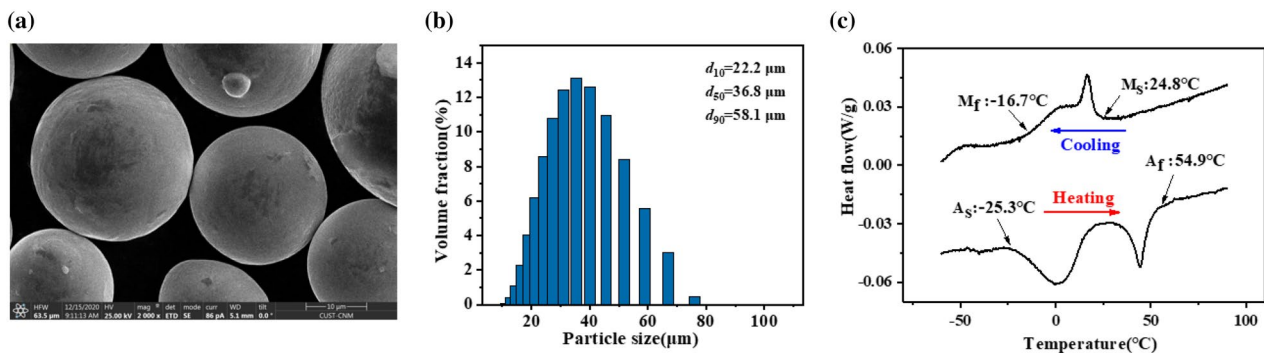

Figure 2 (**a**) Scanning electron microscope image, (**b**) Particle size distribution, (**c**) Differential scanning calorimetry curves for $Ni_{50.8}Ti_{49.2}$ powder

Table 1 Comparison of different energy-absorbing structures

	Geometry configurations	Finite element models	3D printed structure
CS			
DLS			

Yu *et al. Chinese Journal of Mechanical Engineering*　　(2023) 36:104

Page 4 of 10

Table 2 The related parameters of each module material

Parameter	Rigid wall	Solid element	Shell element
P (t/mm^3)	7.83×10^{-9}	6.45×10^{-9}	1×10^{-11}
E (GPa)	207	18.555	210
μ	0.28	0.33	0.3
SIG_ASS (MPa)		188.64	
SIG_ASF(MPa)		353.02	
SIG_SAS(MPa)		126.61	
SIG_SAF(MPa)		57	
EPSL		0.07	

Note: SIG_ASS: Starting value for the forward phase transformation in the case of a uniaxial tensile state of stress. SIG_ASF: Final value for the forward phase transformation in the case of a uniaxial tensile state of stress. SIG_SAS: Starting value for the reverse phase transformation in the case of a uniaxial tensile state of stress. SIG_SAF: Final value for the reverse phase transformation in the case of a uniaxial tensile state of stress. EPSL: Recoverable strain or maximum residual strain.

quasi-static compression. In the finite element model, the S/R quadratic tetrahedron element with Nodal Rotations is used, while the Fully integrated shell element is used in the shell element. Among them, the element size of the CS is 0.3 mm, and the element size of the DLS is 0.1 mm.

After the node set constraint is carried out at the bottom of the model, the rigid wall simulates the load-unload process of the model with the reference to the load curve, so that the numerical simulation can describe its dynamic process relatively accurately. The relevant parameters of each module material are shown in Table 2.

2.3 Additive Manufacturing of Landing Buffer Bionic Model Prototype

Pre-alloyed NiTi powder (Ni: 55.8 wt%) was produced by electrode induction-melting gas atomization (EIGA, Shenzhen Minatech Co. Ltd., China), with particle sizes ranging from 15 to 53 μm (d_{50} of 36.8 μm). The SLM-NiTi (Ni: 55.8 wt%) sample was fabricated from the gas-atomized powder. SLM processing was carried out in argon gas with overpressure of 10–12 mbar and oxygen level below 500 ppm. Eplus M100-T laser processing machine, maximum configuration of 50 μm diameter of 200 W laser. The printing process is as follows:

(1) Before printing, clean the excess powder on the printing platform to ensure that the printing cabin is clean and tidy. Clean the laser lens with a clean cloth dampened with alcohol.
(2) Install the substrate and pour in the NiTi powder.
(3) Replace the new scraper, and then adjust the silo to the appropriate height. Then adjust the scraper and check the installation effect of the scraper.
(4) Put down the air duct, close the hatch door, and carry out the vacuum operation.

(5) Import the model to be printed into the corresponding software and add printing support.
(6) In the operation software, the printing parameters of the sample are set as follows: laser power 120 W, laser scanning speed 600 mm/s, layer thickness 30 μm, and opening spacing 80 μm.

The samples are prepared by the strip partitioning method and the optimized process parameters have good chemical stability, high elastic modulus, high corrosion resistance and shape memory properties. NiTi alloy Ni: 55.8 wt% was used as the fundamental material. Due to the excellent mechanical properties of NiTi shape memory alloy, the obtained microstructure not only has the characteristics of compression, buffering and energy absorption, but also has good recoverability after compression.

2.4 Experimental Details

The Force-Displacement curve was recorded during the quasi-static compressive loading experiment. The prototype was placed in the central position of the experiment bed, and the actual sample experiment process was standardly performed. The Force-Time curve between the static pressure load and the sample was measured by the force sensor. Press down the sample at a rate of 4 mm/min. The temperature in the laboratory is 20 ℃. As shown in Figure 3, the rigid loading plate was pressed on the sample according to the direction of gravity to ensure uniform distribution of impact force.

Phase transformation temperature was studied by using TA Instruments Q20 DSC instrument at a heating/cooling rate of 5 ℃/min from − 70 ℃ to 100 ℃. X-ray diffractometer (XRD, Shimadzu, 6100) was used in analyzing the phase structure. And being compressed at room temperature, the shape memory effect was verified by heating above the A_f point in water at 100 ℃.

3 Results and Discussions

3.1 Phase Structure

As shown in Figure 3(a), the DSC graph shows the M_s is 29.28 ℃, M_f is − 9.66 ℃ upon cooling, and the A_s is 27.81 ℃, A_f is 63.41 ℃ upon heating. And Figure 3(b) shows the XRD pattern of the SLM-NiTi, which demonstrates the sample remains B2 austenite state and B19' martensite state at room temperature (20 ℃), mainly B2 austenite state. The result is consistent with the DSC curve, which proves that the printed material is in B2 austenite state at room temperature with a small amount of B19' martensite phase.

The tensile stress-strain curve of SLM-NiTi is shown in Figure 3(c). The tensile yield strain of the sample is 1.13%, and the yield strength is 193.1 MPa. The fracture strain
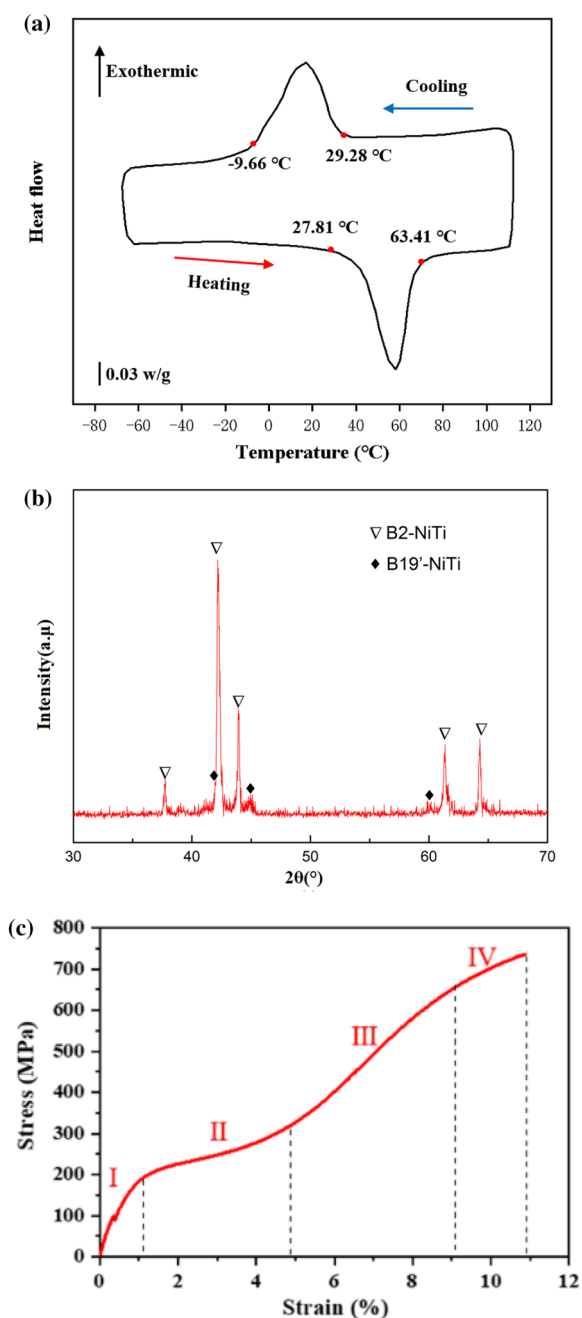
Figure 3 (**a**) DSC graph of the SLM-NiTi, (**b**) XRD pattern of the SLM-NiTi, (**c**) Tensile stress-strain curve at RT

(stage II), the elastic deformation of directional martensite (stage III), and the elastic-plastic deformation of directional martensite (stage IV).

3.2 Deformation Behaviour

Another key measurable output from the finite element simulation and experimental work is the deformation mode of the two structures. Figure 4 shows the deformation process of the quasi-static compressive loading of the CS and DLS. In the early stage of pressure under the rigid loading plate, the unit structure hardly showed obvious deformation due to the strength of NiTi shape memory alloy. Because the CS is placed in the middle of the experiment bed, it is equivalent to restrict the z-direction displacement of the bottom of the bracket only. The energy is absorbed by the structure in a controllable way through regular deformation patterns of the two structures. The deformation modes observed in the experiment are compared with those calculated by finite element simulation.

3.3 Mechanical Properties and Shape Memory Recovery Characteristics

As shown in Figure 5, equivalent von Mises stress and deformed configurations are obtained from FE analysis for two structures. Figure 6(a) and (c) respectively show the FDT curves obtained from the loading-unloading-heating process of the two structures in the simulation analysis and experiment. The two curves can be divided into three parts: loading, unloading and deformation recovery. Firstly, in the loading and unloading part of the curve, the curve of the numerical simulation and the experimental data has a high consistency. As it can be seen, the force-displacement curve is given, the compression process can be divided into two stages. In the first stage, the bearing capacity of the two structures increase with the increase of the compression displacement of relationship, a kind of approximate linear increase in overall is a kind of elastic stage, Stress concentration occurs at the upper part of the CS and the middle joint of the DLS (Figure 5). When the load reaches the value of P_{max} (point B and point B1 of Figure 6), it enters the second stage, and local buckling instability occurs from the upper connection of the CS, resulting in plastic deformation. With the increase of compression displacement, the buckling of the structure gradually diffused to the whole leg. However, before the loading displacement was about 1.1 mm (point B1), the deformation of the DLS was mainly dominated by the elastic deformation of the lower layer bracket. The deformation of the structure increased with the increase of the compression displacement, and the load presented a linear increasing trend. Later, due to excessive structural deformation, the lower support appeared buckling deformation, and the supporting
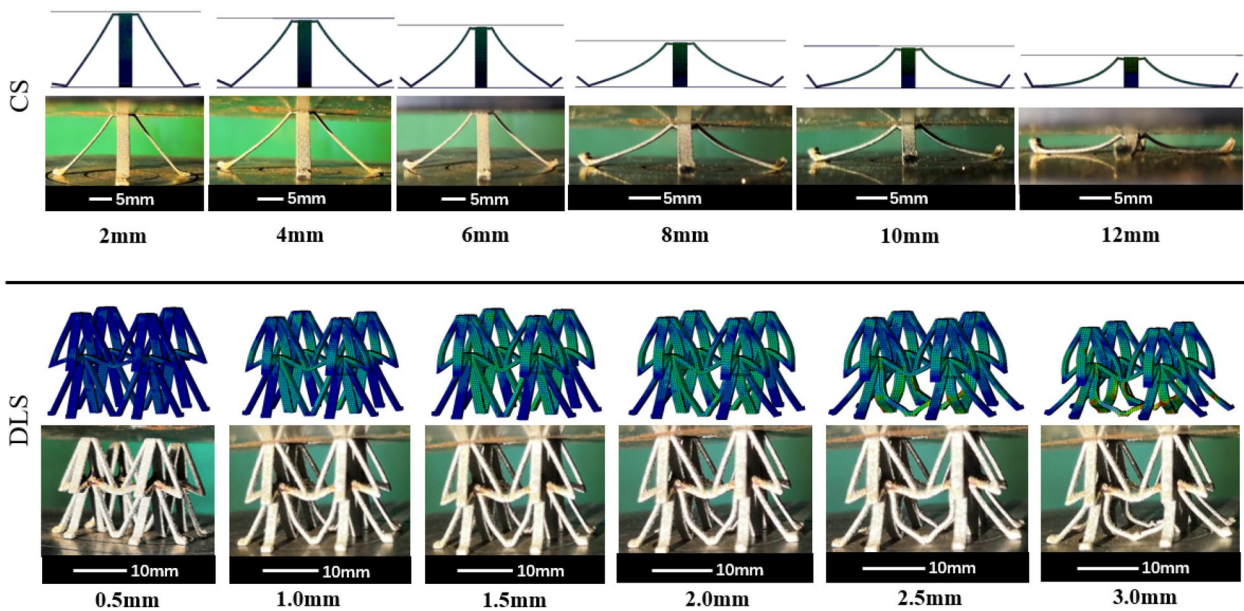
is 10.89% and the fracture strength is 735.18 MPa. It can be seen from the figure that a typical stress platform appears after the yield point due to the martensite orientation deformation during the tensile process. The tensile process of the sample is divided into four stages, which include the initial elastic deformation (stage I), the stress platform caused by martensite orientation deformation

Yu *et al. Chinese Journal of Mechanical Engineering*   (2023) 36:104

Page 6 of 10

Figure 4 Comparisons of the deformation of the bionic structures (CS and DLS) with the computational model
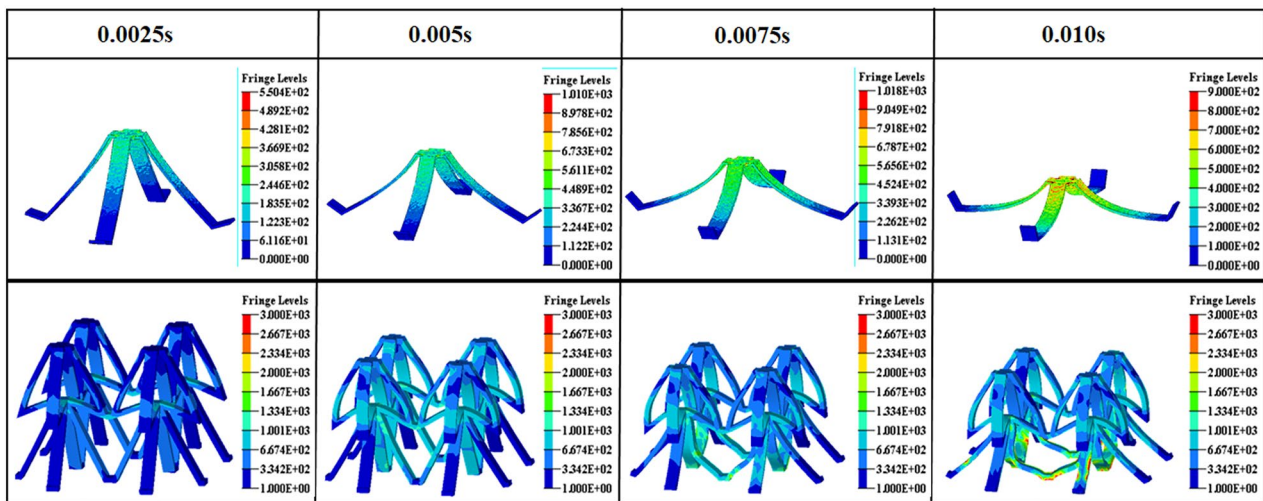

Figure 5 Equivalent von Mises stress and deformed configurations obtained from FE analysis for the bionic structures (CS and DLS)

force of the lower support was dominated by the bending moment of the support (Figure 5). As the bending Angle of the support increases, the supporting force provided by the support became smaller, so the load curve showed a downward trend.

In Figure 6(b), with the reduction of load, the shape of the CS gradually recovered, and elastic recovery rate reached about 84%, This is mainly due to the presence of the B2 austenite phase at room temperature, which gives the material part of the superelasticity, so that it has a certain shape recovery after unloading. It is found that the consistency of the simulation results with the experimental results is close to 90%. The results show that the simulation analysis technique can better simulate the deformation process of the NiTi shape memory alloy double-layer composite module in the process of static crushing, unloading and spring back, to better predict its bearing capacity. After unloading, the elastic recovery rate of the sample reaches 84%. The sample was put into a beaker with hot water (~100 °C), and the SLM-NiTi sample exhibited shape recovery rate of 99%. The reason for the shape recovery after heating is that part of the B19' martensite has undergone heat-induced martensite transformation. It can be inferred that although the total
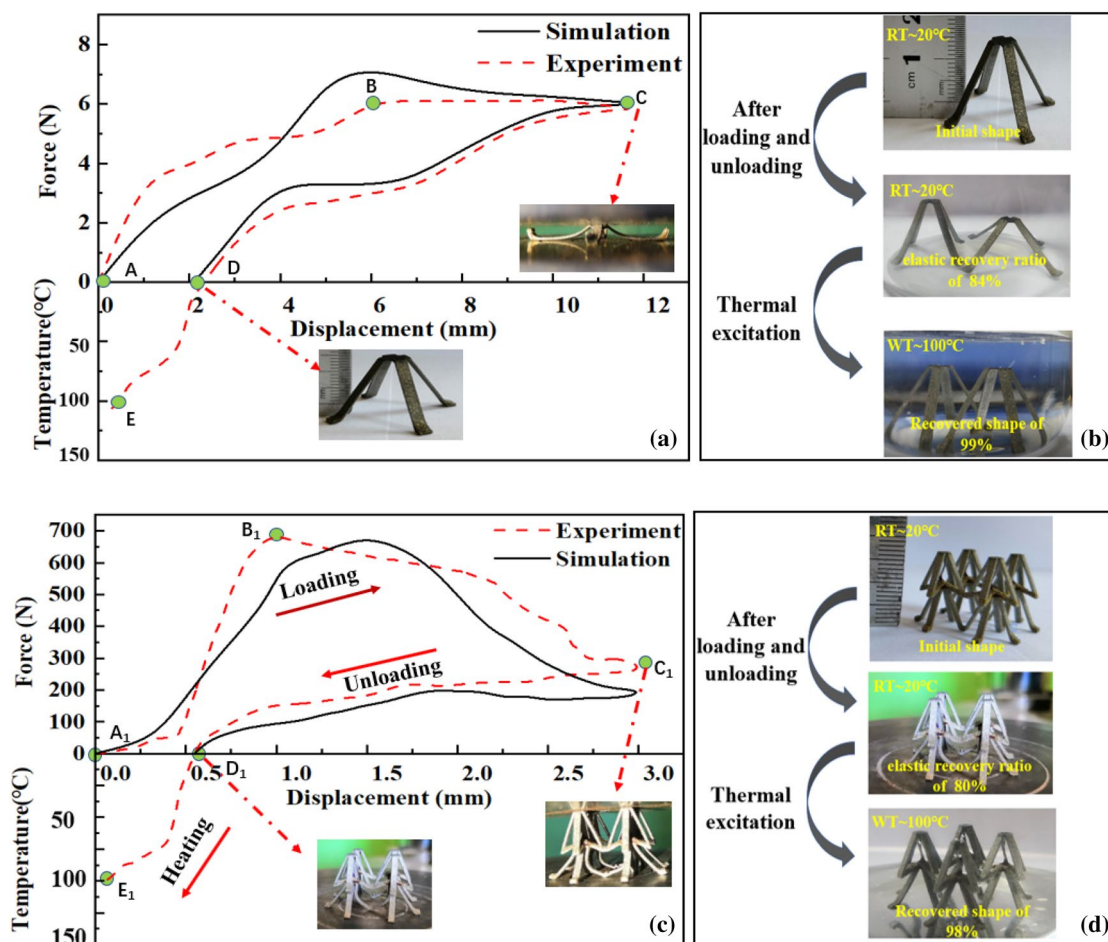
Figure 6 (**a**) FDT curves acquired through a loading-unloading-heating process of the CS, (**b**) Shape recovery process of the CS after being heated in a water bath after deformation, (**c**) FDT curves obtained by loading-unloading-heating processes of the DLS, (**d**) Shape recovery process of the DLS after being heated in a water bath after deformation

deformation is 70%, the deformation in some areas is much lower than 70%, and it may have only undergone martensitic transformation redirection without plastic deformation. Therefore, the deformed part can be restored to its original shape after heating.

In Figures 5 and 6(d), the compression process and experimental results of the DLS were further analyzed. In the process of pressing the rigid plate, the deformation first appears in the lower bracket, and the edge of the lower bracket opens to the surrounding. While the upper bracket does not show obvious deformation, indicating that the strength of the upper bracket is obviously greater than that of the lower bracket. When pressing down for 3 mm, the lap positions of the upper and lower brackets become brittle, resulting in structural instability and the end of the experiment. In this scheme, the support has a thickness of 0.6 mm, a width of 1.5 mm and a thickness to width ratio of 2:5. In the future, the thickness to width ratio will be reduced, and the support will be designed to

be a structure similar to a thin plate as possible to give full play to its hyperelasticity characteristics and to avoid premature brittle fracture of the 3D printed structure. Also, compression loading should be withdrawn after the downforce displacement reaches 3 mm. In a word, the deformation order of the structure is basically bottom-up. Therefore, in order to improve the bearing capacity of the whole structure or control the deformation sequence of the structure, a support with the lower strength should be chosen. In this study, quasi-static compression loading simulation analysis is carried out on the two-layer module to simulate the entire deformation process of the module during the loading stage. This work will provide the basis for the optimization of nickel-titanium alloy in multi-variable and multi-parameter module.

There is a slight difference between the simulation analysis and the experiment during loading. Before the loading displacement was about 1.1 mm (point B), the deformation of the double-layer structure was mainly

Yu *et al. Chinese Journal of Mechanical Engineering*   (2023) 36:104

Page 8 of 10

dominated by the elastic deformation of the lower layer bracket. The deformation of the structure increased with the increase of the compression displacement, and the load presented a linear increasing trend. Later, due to excessive structural deformation, the lower support appears buckling deformation, and the supporting force of the lower support is dominated by the bending moment of the support. As the bending Angle of the support increases, the supporting force provided by the support becomes smaller, so the load curve shows a downward trend. The final state after unloading is similar to the CS. As shown in Figure 6(a) and (c), when the structure produces shape memory recovery under the action of thermal excitation, the structure under the deformation state exhibits different recovery efficiency at different temperatures. In experiment, we observed that the DLS rapidly recovered its shape within a few seconds after being stimulated by heat and achieved a recovery rate of about 98%. Therefore, it can be concluded that the DLS has excellent reusable performance.

3.4 Performance Indicators

Different parameters are used to compare the performance of various devices. The indicators used within this study include peak force (P_{max}); energy absorption (EA); specific energy absorption (SEA); and shape recovery rate.

The P_{max} is the force required to initiate plastic deformation within the tube and hence begin the energy absorption. Total energy absorption through plastic deformation is calculated as the area under the force-displacement curve, using Eq. (1):

$$EA = \int_0^d P(x)\mathrm{d}x, \tag{1}$$

where d is the total structural volume, P is static force, x is the instantaneous crush displacement.

Given that mass is a key indicator in any automotive structural design, specific energy absorption provides an indicator of the EA per unit mass, as presented in Eq. (2). A high EA and SEA are highly desirable within crashworthy applications:

$$SEA = \frac{EA}{M}, \tag{2}$$

where M is the structural mass.

3.5 Post-Compression Analysis

The experimental percentage crush and corresponding reaction force were generated from the experiment machine. The recorded Performance indicators are listed

Table 3 Comparison of crashworthiness indicators for quasi-static compressive loading

Crashworthiness indicators	CS	DLS
M (g)	0.969	2.372
EA (J)	0.268	27.71
SEA (J/g)	0.277	11.682
P_{max} (N)	7.2	634
Shape recovery rate (%)	99	98
Compressible strain (%)	66.67	17.65

in Table 3, including the P_{max}, EA, SEA, M, compressible rate and shape recovery rate.

From Table 3, it may be observed that DLS has excellent mechanical properties, but its compressible deformation is small. On the contrary, although CS has weak mechanical properties, its compressible deformation can reach 66.67%, and its shape recovery rate can reach 99% after thermal excitation.

4 Conclusions

In this paper, a recoverable NiTi alloy landing buffer bionic structure system was developed with the inspiration of the excellent impact energy absorption of Odontodactylus scyllarus's predatory feet. presents a comprehensive investigation of the crashworthiness of simple hierarchical and fractal hierarchical structures using experimental experiments and computational modeling techniques. Several conclusions are drawn from the results:

(1) It is of great theoretical and practical significance to improve the structure of lander shock absorber by printing biomimetic model based on additive manufacturing technology. The structure is based on Nitinol and has a good shape memory recovery performance, which provides an effective solution to the efficient reuse of the lander. This is the key to achieving continuous protection after any initial interference.

(2) The experiment and simulation of the unit structure show that the CS has a very high elasticity although it is not outstanding in carrying capacity, which provides a good idea for the study of buffer structure. When the bionic DLS is pressed down by about 38.9%, the peak load of the DLS is 692 N. Compared with the CS, in the loading and unloading process, the DLS shows a higher capacity of load and absorption.

(3) This study helps us understand the deformation pattern and interlayer strength distribution of each

Yu *et al. Chinese Journal of Mechanical Engineering*   (2023) 36:104

Page 9 of 10

structure, provides an important basis for the optimal design of each layer and the deformation control of the entire module, and lays a foundation for the extended application and performance design of multi-layer NiTi alloys.

Authors' Contributions
ZY, ZZ and PL is in charge of the whole trial; RX wrote the manuscript; ZX assisted with sampling and laboratory analyses. YZ, XZ, is in charge of the investigation. SH is in charge of the Supervision. All authors read and approved the final manuscript.

Authors' Information
Zhenglei Yu, born in 1984, a professor of *Key Laboratory of Bionic Engineering, Ministry of Education, Jilin University, China*. In 2014, he graduated from *School of Mechanical Science and Engineering, Jilin University, China* with a doctorate degree. His research interests include bionic structure design and additive manufacturing technology.
Renlong Xin, born in 1997, graduated from *Shandong University of Technology, China*. In the same year, he entered *Key Laboratory of Bionic Engineering, Ministry of Education, Jilin University, China* for his master's degree.
Zezhou Xu, born in 1995, is currently a PhD candidate at *Key Laboratory of Bionic Engineering, Ministry of Education, Jilin University, China*. His research interests include additive manufacturing of NiTi alloy.
Yining Zhu, born in 2002, is currently a master candidate at *Animal Science, Yanbian University, China*.
Xiaolong Zhang, born in 1996, is currently a PhD candidate at *Key Laboratory of Bionic Engineering, Ministry of Education, Jilin University, China*. His research interests include bionic structure design and additive manufacturing.
Shijie Hao, born in 1984, a professor of *State Key Laboratory of Heavy Oil Processing, China University of Petroleum, China*, he was selected as "Young Changjiang Scholars" by the Ministry of Education of China in 2015. Now, his main research direction is high-performance shape memory alloy composite materials and 3D printing shape memory alloy.
Zhihui Zhang, born in 1976, a professor of *Key Laboratory of Bionic Engineering, Ministry of Education, Jilin University*, *China*. He graduated from *Jilin University, China*, in 2007 and majored in material processing engineering. Now he is the Vice Dean of *College of Biological and Agricultural Engineering, Jilin University, China*. He has presided over the National Key Research and Development Program and Key Projects of National Natural Science Foundation.
Ping Liang, born in 1965, a professor of *Key Laboratory of Bionic Engineering, Ministry of Education, Jilin University*, *China*. His research interests include bionics, solid mechanics and fluid mechanics.

Availability of Data and Materials
The data and materials that support the findings of this study are available from the corresponding author upon reasonable request.

Declarations

Competing Interests
We declare that we have no financial and personal relationships with other people or organizations that can inappropriately influence our work, there is no professional or other personal interest of any nature or kind in any product, service and/or company that could be construed as influencing the position presented in, or the review of the manuscript entitled.

References
[1]   F M Zeng, J Z Yang, W Zhu, et al. Research on design method of lunar Lander landing buffer mechanism. *Spacecraft Engineering*, 2010, 20: 46-51.
[2]   Z Yan. *Design and analysis of outrigger buffers for vtol reusable launch vehicles*. Harbin: Harbin Institute of Technology, 2019. (in Chinese)
[3]   S V Wal, R G Reid, D J Scheeres. Simulation of nonspherical asteroid landers: Contact modeling and shape effects on bouncing. *Journal of Spacecraft and Rockets*, 2020, 57: 109-130.
[4]   Z Y Chen, M Imholz, L Li, et al. Transient landing dynamics analysis for a lunar lander with random and interval fields. *Applied Mathematical Modeling*, 2020, 88: 827-851.
[5]   R F Li, W Z Guo. Novel design of a family of legged mobile landers based on decoupled landing and walking functions. *Journal of Mechanical Science and Technology*, 2020, 34: 3851-3822.
[6]   M Y Huang. Control strategy of launch vehicle and lander with adaptive landing gear for sloped landing. *Acta Astronautica*, 2019, 161: 509-523.
[7]   M T Ababneh, C Tarau, W G Anderson, et al. Thermal control of lunar and mars rovers/landers using hybrid heat pipes. *Journal of Thermophysics and Heat Transfer*, 2019, 33: 705-713.
[8]   B Cheng, Y Yu, H X Baoyin. Numerical simulations of the controlled motion of a hopping asteroid lander on the regolith surface. *Monthly Notices of the Royal Astronomical Society*, 2019, 485: 3088-3096.
[9]   T Maeda, M Otsuki, T Hashimoto. Protection against overturning of a lunar-planetary lander using a controlled landing gear. *Aerospace Engineering*, 2019, 233: 438-456.
[10]   L Witte, R Roll, J Biele, et al. Rosetta lander Philae - Landing performance and touchdown safety assessment. *Acta Astronautica*, 2016, 125: 149-160.
[11]   J Rivera, M S Hosseini, D Restrepo, et al. Toughening mechanisms of the elytra of the diabolical ironclad beetle. *Nature*, 2020, 586(7830): 543-548.
[12]   J Zhang, W Chen, M Yang, et al. The Ingenious Structure of Scorpion Armor Inspires Sand-Resistant Surfaces. *Tribology Letters*, 2017, 65(3): 110.
[13]   C Gong, Z H Bai, J Y Lv, et al. Crashworthiness analysis of bionic thin-walled tubes inspired by the evolution laws of plant stems. *Thin-Walled Structures*, 2020, 157: 107081.
[14]   T Claverie, E Chan, S N Patek. Modularity and scaling in fast movements: Power amplification in mantis shrimp. *Evolution*, 2011, 65: 443-461.
[15]   S N Patek, R L Caldwell. Extreme impact and cavitation forces of a biological hammer: Strike forces of the peacock mantis shrimp mantis shrimp. *Journal of Experimental Biology*, 2005, 208: 3655-3664.
[16]   K Knight. Mantis shrimp pull punches in air for self-preservation. *Journal of Experimental Biology*, 2020, 223.
[17]   S N Patek. The power of mantis shrimp strikes: Interdisciplinary impacts of an extreme cascade of energy release. *Integrative and Comparative Biology*, 2019, 59: 1573-1585.
[18]   J C Weaver, G W Milliron, A Miserez, et al. The Stomatopod Dactyl Club: A formidable damage-tolerant biological hammer. *Science*, 2012, 336: 1275-1280.
[19]   X Guo, X J Dong, Z L Yu, et al. Study on the mechanical properties of bionic protection and self-recovery structures. *Materials*, 2020, 13.
[20]   Z L Yu, Z Z Xu, Y T Guo, et al. Study on properties of SLM-NiTi shape memory alloy under the same energy density. *Journal of Materials Research and Technology*, 2021, 13: 241-250.
[21]   G F Yao, R Y Liu, Z Z Xu, et al. Study on quasi-static mechanical properties of four 3D-printed bio-inspired structures based on functional relationship. *Composite Structures*, 2021, 274(15): 114304.
[22]   F Xiong, H F Yang, K Liu, et al. Forming and two-way shape memory effect of NiTi alloy induced by laser shock imprinting. *Optics and Laser Technology*, 2019, 120.
[23]   B A Bimber, R F Hamilton, J Keist, et al. Anisotropic microstructure and superelasticity of additive manufactured NiTi alloy bulk builds using laser

directed energy deposition. *Materials Science & Engineering A*, 2016, 674: 125-134.

[24] M Elahinia, N S Moghaddam, M T Andani, et al. Fabrication of NiTi through additive manufacturing: A review. *Progress in Materials Science*, 2016, 83: 630-663.

[25] C A Biffi, P Bassani, J Fiocchi, et al. Microstructural and mechanical response of NiTi lattice 3D structure produced by selective laser melting. *Metals*, 2020, 10.

[26] V Humbeeck Jan. Additive manufacturing of shape memory alloys. *Shape Memory and Superelasticity*, 2018, 04: 309-312.

[27] M T Andani, S Saedi, A S Turabi, et al. Mechanical and shape memory properties of porous $Ni_{50.1}Ti_{49.9}$ alloys manufactured by selective laser melting. *Journal of the Mechanical Behavior of Biomedical Materials*, 2017, 68: 224-231.

[28] M Speirs, B Van Hooreweder, J Van Humbeeck, et al. Fatigue behaviour of NiTi shape memory alloy scaffolds produced by SLM, a unit cell design comparison. *Journal of the Mechanical Behavior of Biomedical Materials*, 2017, 70: 53-59.

[29] S Dadbakhsh, M Speirs, J P Kruth, et al. Influence of SLM on shape memory and compression behaviour of NiTi scaffolds. *CIRP Annals - Manufacturing Technology*, 2015, 64: 209-212.

[30] C L Ma, D D Gu, K J Lin, et al. Selective laser melting additive manufacturing of cancer pagurus's claw inspired bionic structures with high strength and toughness. *Applied Surface Science*, 2019, 469: 647-656.

[31] Z W Xiong, Z H Li, Z Sun, et al. Selective laser melting of NiTi alloy with superior tensile property and shape memory effect. *Journal of Materials Science & Technology*, 2019, 35: 2238-2242.